

Optimization of the Multigrid-Convergence Rate on Semi-structured Meshes by Local Fourier Analysis

B. Gmeiner^{1,a}, T. Gradl^{1,a}, F. Gaspar^{1,b}, U. Rde^{1,a}

^a*Department of Computer Science, System Simulation, Cauerstr. 11, 91058 Erlangen, Germany*

^b*Department of Applied Mathematics, University of Zaragoza. Pedro Cerbuna 12, 50009 Zaragoza, Spain*

Abstract

In this paper a local Fourier analysis for multigrid methods on tetrahedral grids is presented. Different smoothers for the discretization of the Laplace operator by linear finite elements on such grids are analyzed. A four-color smoother is presented as an efficient choice for regular tetrahedral grids, whereas line and plane relaxations are needed for poorly shaped tetrahedra. A novel partitioning of the Fourier space is proposed to analyze the four-color smoother. Numerical test calculations validate the theoretical predictions. A multigrid method is constructed in a block-wise form, by using different smoothers and different numbers of pre- and post-smoothing steps in each tetrahedron of the coarsest grid of the domain. Some numerical experiments are presented to illustrate the efficiency of this multigrid algorithm.

Keywords: multigrid, local Fourier analysis, convergence rate, smoothers

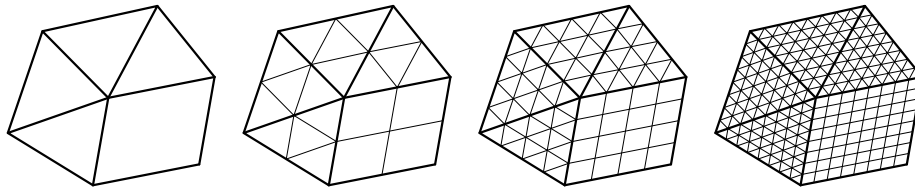
1. Introduction and terminology

Multigrid (MG) methods [10, 18, 32, 33] are known to have optimal computational complexity for solving many numerical problems. However, in practice their performance in solving individual problems varies significantly. The speed of convergence towards a solution depends on the numerical properties of the underlying problem, e. g., the type of a differential equation and the method used for discretizing the equation. Besides that, the user can choose from a variety of algorithms for the components of the MG method, most prominently the smoother, the restriction, and the prolongation. Choosing the appropriate components for a specific problem has also a great impact on the overall performance.

For solving elliptic PDEs, finite element methods are often preferred over other discretization schemes, because they permit the use of flexible, unstruc-

Email addresses: bjoern.gmeiner@cs.fau.de (B. Gmeiner), tobias.gradl@cs.fau.de (T. Gradl), fjgaspar@unizar.es (F. Gaspar), ulrich.uede@cs.fau.de (U. Rde)

Figure 1: Regular refinement example for a two-dimensional input mesh. Beginning with the input mesh on the left, each successive level of refinement creates a new mesh that has a larger number of interior points with structured couplings.



tured meshes. Algebraic multigrid (AMG) methods [9, 29, 31, 32] inherently support unstructured meshes by construction. BoomerAMG from the Hypre package is a popular implementation of AMG [20]. Geometric multigrid, in contrast, relies on a given hierarchy of nested meshes. Geometric multigrid may achieve a significantly higher performance than algebraic multigrid in terms of unknowns computed per second.

The Hierarchical Hybrid Grids (HHG) software framework [3, 17] is designed to close this gap between finite element flexibility and geometric multigrid performance by using a compromise between structured and unstructured grids. A coarse input finite element mesh is organized into grid primitives vertices, edges, faces, and volumes. The primitives are then refined in a structured way, as indicated in Figure 1 for the two-dimensional case. In the case of tetrahedral grids, Bey’s refinement strategy will be considered [5]. There each input tetrahedron is subdivided into eight child tetrahedra of equal volume, in such a way that each corner of a child coincides to either a corner or an edge midpoint of the parent. The accuracy of tetrahedral finite elements w.r.t. their maximal angle is discussed e.g. in [24]. The HHG data layout preserves the flexibility of unstructured meshes, while the regular internal structure of the primitives allows for an efficient implementation on current computer architectures, especially on parallel computers. In parallel runs on up to 294 912 cores, HHG has demonstrated excellent performance for solving linear systems with up to 10^{12} unknowns [16]. Semi-structured meshes also support a local tuning of the smoothing parameters as will be discussed later in this paper.

Generally the design of MG algorithms and their components should be based on a careful performance analysis. Such an analysis could be based in the comparison of convergence rates of different algorithmic variants. For standard cases, such as the 7-point stencil for the Laplace operator in 3D, convergence rates are reported in the literature. In our case, however, we will use 15-point stencils as they arise in the HHG framework with tetrahedral finite elements.

Local Fourier analysis (LFA) [8] is a very useful tool to predict the asymptotic convergence factors of MG methods with high accuracy quantitatively. Therefore it is widely used to design efficient MG algorithms. In the LFA an infinite regular grid is considered and boundary conditions are ignored. On an infinite grid, the discrete solution and the corresponding error can be represented by linear combinations of certain complex exponential functions, the

Fourier modes, which form a unitary basis of the space of grid functions with bounded l_2 -norm. The LFA monograph of Wienands and Joppich [34] provides an excellent background for experimenting with Fourier analysis. Recent advances in this context include LFA for hexagonal meshes [38], multigrid as a preconditioner [35], optimal control problems [6], and discontinuous Galerkin discretizations [19]. In [7], an LFA for multigrid methods for the finite element discretization of the two-dimensional curl-curl equation on a quadrilateral grid has been introduced. Recently a generalization of the LFA to triangular grids has been proposed in [13] for a two-dimensional scalar problem. The key to carrying out this generalization is to express the Fourier transform in a special coordinate system. Our aim in this paper is to show that it is possible to perform an LFA also on 3-dimensional tetrahedral grids so that we can use it to design efficient multigrid solvers in the HHG framework. To choose suitable components of the multigrid method, the LFA will be applied for each tetrahedron of the input mesh in such a way that the global behavior of the method becomes as efficient as possible.

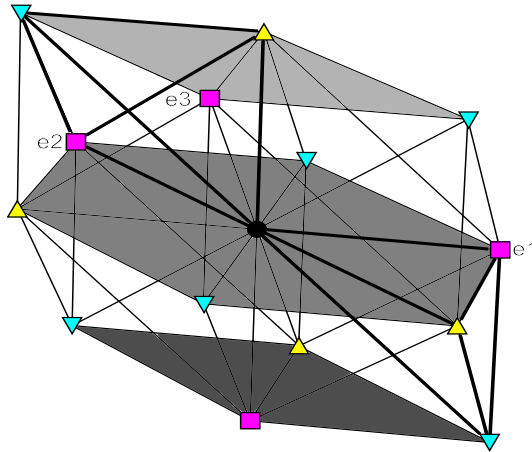
In a multigrid algorithm, the smoother has the task to reduce the high-frequency error components, while the coarse-grid correction reduces the low-frequency components. Both, smoother and coarse-grid correction [12, 26] can be tuned to optimally suit the numerical problem, i. e. the differential equation and its discretization. In this paper, we focus on optimizing the smoother depending on the shape of the tetrahedra. Besides choosing the smoother type, two more parameters can be changed to achieve more efficient smoothing behavior: the under-/over-relaxation parameter (ω) and the number of pre-/post-smoothing steps per multigrid cycle (ν_1, ν_2). All the parameters can even be adapted locally to the problem, if the numerical properties differ strongly across the domain.

The Gauss-Seidel algorithm often is a better smoother than the Jacobi algorithm, but due to its data dependencies, it is potentially slower. The data dependencies can be eliminated by coloring the grid points such that points of the same color are not directly connected to each other, and can thus be updated in parallel. In a 2D rectangular grid with a 5-point discretization stencil, e.g. two colors are needed, whereas the 15-point stencil within HHG solver requires four colors, see Figure 2. Note that a relaxation parameter ω can be chosen individually for each of the colors ($\omega_i = \omega_1, \omega_2, \omega_3, \omega_4$).

In this work, a linear finite element discretization of the Laplace equation will be analyzed and, as we will see, four-color relaxation results in a very efficient smoother for regular tetrahedral grids. However, when poorly shaped tetrahedra occur, then point-wise smoothers are not efficient anymore. In this case we will consider block-wise smoothers. In particular, line- and plane-wise smoothers will be used. Note that for Bey refinement, seven different line smoothers can be defined that correspond with the seven directions that appear in the connections between each pair of stencil entries, see Figure 2. Similarly, seven different plane smoothers can be considered. Four faces have the orientation of the un-refined tetrahedron face. Three other face orientations can be spanned up by two vectors connecting two opposing edges. The remaining multigrid components

will be standard, i.e. we will use linear interpolation and its adjoint as transfer operators and will use Galerkin coarsening for defining the coarse-grid operators.

Figure 2: Coloring of a 15-point stencil. Four different colors (and shapes accordingly) are used to break all dependencies between each connected pair of vertices. Planes between the elements are introduced to improve readability. Exemplary two tetrahedra are shown with thicker edges.



The organization of the remaining paper is as follows. In Section 2 we present the local Fourier analysis for tetrahedral grids. The key here is to consider a basis of the function space appropriate for the structure of the grid. In Section 3, a four-color smoother is defined for which smoothing and two-grid analysis will be performed. In this study, an important aspect is to show the decomposition of the Fourier space into minimal invariant subspaces. These are four-dimensional for the smoothing analysis and have sixteen dimensions for the two-grid analysis.

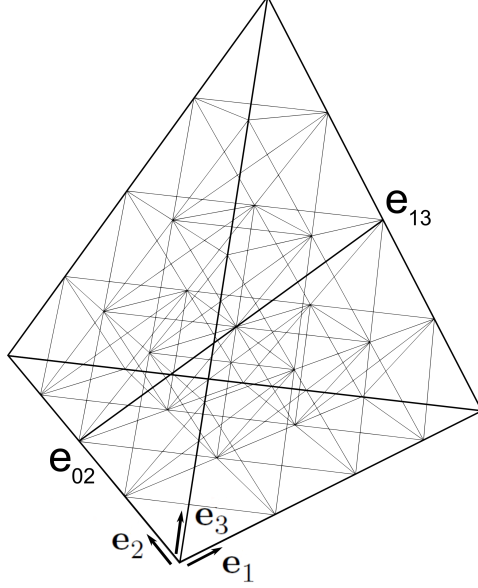
Section 4 is devoted to Fourier analysis results for the Laplace operator discretized by linear finite elements on tetrahedral grids. Different smoothers will be proposed depending on the particular geometry of the grid on each tetrahedral patch. It will be shown that a four-color smoother will be the best choice for regular tetrahedra. Otherwise block smoothers may be more suitable, for instance line-smoothers or zebra-plane smoothers. Finally, in Section 5 numerical experiments will show that for domains composed of different types of tetrahedra, a prescribed global convergence factor, can be obtained using the local LFA predictions on each tetrahedron of the input grid.

2. Local Fourier analysis

2.1. General definitions

In this section we extend the local Fourier analysis to multigrid methods on regular tetrahedral grids. The key to accomplishing this is to use the three-

Figure 3: Regular tetrahedral grid



dimensional discrete Fourier transform using coordinates in non-orthogonal bases fitting the structure of the grid.

Given $\mathbf{h} = (h_1, h_2, h_3)$ a grid spacing, let \mathcal{T}_h be a regular tetrahedral grid on a fixed coarse tetrahedron \mathcal{T} and let $\{\mathbf{e}_1, \mathbf{e}_2, \mathbf{e}_3\}$ be unit vectors indicating the direction of three of the edges of \mathcal{T} ; see Figure 3. We extend \mathcal{T}_h to the infinite grid

$$G_h = \{\mathbf{x} = x_1\mathbf{e}_1 + x_2\mathbf{e}_2 + x_3\mathbf{e}_3 \mid x_i = k_i h_i, k_i \in \mathbf{Z}, i = 1, 2, 3\}, \quad (1)$$

such that $\mathcal{T}_h = G_h \cap \mathcal{T}$. We write the Fourier frequencies as $\boldsymbol{\theta} = \theta_1\mathbf{e}'_1 + \theta_2\mathbf{e}'_2 + \theta_3\mathbf{e}'_3$, where $\{\mathbf{e}'_1, \mathbf{e}'_2, \mathbf{e}'_3\}$ is the reciprocal basis to $\{\mathbf{e}_1, \mathbf{e}_2, \mathbf{e}_3\}$, i. e., $\mathbf{e}_i \cdot \mathbf{e}'_j = \delta_{ij}$. In this way, the back Fourier transformation has an expression similar to that in Cartesian coordinates. Therefore, every bounded grid function $u_h(\mathbf{x})$ defined on G_h can be written as a formal linear combination of the discrete complex exponential functions called Fourier modes

$$\varphi_h(\boldsymbol{\theta}, \mathbf{x}) = e^{i(\theta_1 x_1 + \theta_2 x_2 + \theta_3 x_3)}, \quad (2)$$

where the Fourier frequencies $\boldsymbol{\theta} = \theta_1\mathbf{e}'_1 + \theta_2\mathbf{e}'_2 + \theta_3\mathbf{e}'_3$ vary continuously in \mathbf{R}^3 . Since $\varphi_h(\tilde{\boldsymbol{\theta}}, \mathbf{x}) = \varphi_h(\boldsymbol{\theta}, \mathbf{x})$ for all $\mathbf{x} \in G_h$ if and only if $\tilde{\theta}_i = \theta_i \pmod{2\pi/h_i}$, $i = 1, 2, 3$, the too high frequencies are not visible on grid G_h due to aliasing effects. These are the Fourier modes with associated frequency $\boldsymbol{\theta}$ such that for some component $|\theta_i| \geq \pi/h_i$. Therefore, the Fourier space

$$\mathcal{F}(G_h) = \text{span}\{\varphi_h(\boldsymbol{\theta}, \cdot) \mid \boldsymbol{\theta} = (\theta_1, \theta_2, \theta_3) \in \boldsymbol{\Theta}_h\},$$

with $\Theta_h = (-\pi/h_1, \pi/h_1] \times (-\pi/h_2, \pi/h_2] \times (-\pi/h_3, \pi/h_3]$, contains any infinite grid function on G_h with bounded l2-norm. If regular refinement is applied, we are considering the case of standard multigrid coarsening, $(H_1, H_2, H_3) = (2h_1, 2h_2, 2h_3)$, and therefore the infinite coarse grid G_H is defined as

$$G_H = \{\mathbf{x} = x_1 \mathbf{e}_1 + x_2 \mathbf{e}_2 + x_3 \mathbf{e}_3 \mid x_i = 2k_i h_i, k_i \in \mathbf{Z}, i = 1, 2, 3\}.$$

We distinguish high and low frequencies on G_h with respect to G_H . We define the subset Θ_H of low frequencies as $\Theta_H = (-\pi/H_1, \pi/H_1] \times (-\pi/H_2, \pi/H_2] \times (-\pi/H_3, \pi/H_3]$, and the subset of high frequencies $\Theta_h \setminus \Theta_H$. This definition is based on the fact that only low frequencies are visible on the coarse grid G_H . Each high-frequency component coincides with a certain low-frequency component on G_H . In particular we have $\varphi_h(\tilde{\boldsymbol{\theta}}, \cdot) = \varphi_h(\boldsymbol{\theta}, \cdot)$ on G_H with $\tilde{\theta}_i = \theta_i \pmod{\pi/h_i}, i = 1, 2, 3$.

The discrete operators considered here are assumed to be linear with constant coefficients. Neglecting boundary conditions and/or connections with other neighboring tetrahedra on the coarsest grid, the discrete problem $L_h u_h = f_h$ can be extended to the whole grid G_h . For a fixed grid point $\mathbf{x} = (x_1, x_2, x_3) \in G_h$, the corresponding equation reads in stencil notation as

$$L_h u_h(\mathbf{x}) = \sum_{\mathbf{k} \in \mathcal{I}} s_{\mathbf{k}} u_h(x_1 + k_1 h_1, x_2 + k_2 h_2, x_3 + k_3 h_3) = f_h(\mathbf{x}), \quad (3)$$

where $s_{\mathbf{k}} \in \mathbf{R}$ are constant coefficients and $\mathcal{I} \subset \mathbf{Z}^3$ is a finite index set. From (3), it can be deduced that the grid-functions $\varphi_h(\boldsymbol{\theta}, \mathbf{x})$ given in (2) are formal eigenfunctions of the discrete operator L_h . More precisely, the relation $L_h \varphi_h(\boldsymbol{\theta}, \mathbf{x}) = \widehat{L}_h(\boldsymbol{\theta}) \varphi_h(\boldsymbol{\theta}, \mathbf{x})$ holds, where

$$\widehat{L}_h(\boldsymbol{\theta}) = \sum_{\mathbf{k} \in \mathcal{I}} s_{\mathbf{k}} e^{i(\theta_1 k_1 h_1 + \theta_2 k_2 h_2 + \theta_3 k_3 h_3)}$$

is the corresponding eigenvalue or Fourier symbol of L_h .

2.2. Smoothing analysis

Recall that one of the basic concepts of multigrid methods is the assumption that high-frequency error components are smoothed by relaxation, and the low-frequency error components are reduced by coarse grid correction. In Fourier smoothing analysis, the influence of a smoothing operator S_h on the high-frequency error components is investigated. There an ideal coarse-grid operator is assumed which annihilates the low frequency error components and leaves the high frequency components unchanged.

Smoothing procedures, such as Gauss-Seidel, line or plane smoothers, have the property that all $\varphi_h(\boldsymbol{\theta}, \cdot)$ are eigenfunctions of the smoothing operator. In this case, the definition of the smoothing factor is given by

$$\mu(S_h) = \sup_{\boldsymbol{\theta} \in \Theta_h \setminus \Theta_H} |\widehat{S_h}(\boldsymbol{\theta})| \quad (4)$$

The situation is more difficult for the four-color relaxation mentioned in Section 1, as the Fourier components are not eigenfunctions of the relaxation operator. Section 3 is devoted to a detailed analysis of this smoother.

2.3. Two-grid analysis

In order to investigate the interplay between relaxation and coarse grid correction, which is crucial for an efficient multigrid method, it is necessary to perform a two-grid analysis which takes into account the effect of transfer operators. Let u_h^m be an approximation of u_h . The error $e_h^m = u_h^m - u_h$ is transformed by a two-grid cycle as $e_h^{m+1} = M_h^H e_h^m$, where $M_h^H = S_h^{\nu_2} K_h^H S_h^{\nu_1}$ is the two-grid operator, $K_h^H = I_h - P_H^h (L_H)^{-1} R_h^H L_h$ the coarse grid correction operator and S_h is a smoothing operator on G_h with ν_1 and ν_2 indicating the number of pre- and post-smoothing steps, respectively. In the definition of K_h^H , L_H is the coarse grid operator and P_H^h, R_h^H are transfer operators from coarse to fine grids and vice versa. The two-grid analysis is the basis for the classical asymptotic multigrid convergence estimates, and the spectral radius $\rho(M_h^H)$ of the operator M_h^H indicates the asymptotic convergence factor of the two-grid method.

The Fourier space $\mathcal{F}(G_h)$ is decomposed into eight-dimensional subspaces $\mathcal{F}^8(\boldsymbol{\theta}^{000})$, known as $2h$ -harmonics, which are generated by the Fourier modes corresponding to one low-frequency harmonic $\boldsymbol{\theta}^{000} \in \Theta_H$ with coordinates $\boldsymbol{\theta}^{000} = (\theta_1^{000}, \theta_2^{000}, \theta_3^{000})$ and seven corresponding high-frequency harmonics in $\Theta_h \setminus \Theta_H$:

$$\begin{aligned} \mathcal{F}^8(\boldsymbol{\theta}^{000}) &= \text{span}\{\varphi_h(\boldsymbol{\theta}^{\alpha_1 \alpha_2 \alpha_3}, \cdot) \mid \alpha_1, \alpha_2, \alpha_3 \in \{0, 1\}\} \text{ with } \boldsymbol{\theta}^{000} \in \Theta_H, \\ \boldsymbol{\theta}^{\alpha_1 \alpha_2 \alpha_3} &= \boldsymbol{\theta}^{000} - (\alpha_1 \text{sign}(\theta_1^{000})\pi/h_1, \alpha_2 \text{sign}(\theta_2^{000})\pi/h_2, \alpha_3 \text{sign}(\theta_3^{000})\pi/h_3). \end{aligned} \quad (5)$$

In order to ensure that we deal with non-singular Fourier symbols $\widehat{L}_h(\boldsymbol{\theta})$ and $\widehat{L}_H(2\boldsymbol{\theta})$, we restrict our considerations to the subspace

$$\mathcal{F}(G_h) \setminus \bigcup_{\boldsymbol{\theta}^{000} \in \Psi} \mathcal{F}^8(\boldsymbol{\theta}^{000}),$$

with $\Psi = \{\boldsymbol{\theta}^{000} \in \Theta_H \mid \widehat{L}_H(2\boldsymbol{\theta}^{000}) = 0 \text{ or } \widehat{L}_h(\boldsymbol{\theta}^{\alpha_1 \alpha_2 \alpha_3}) = 0, \alpha_1, \alpha_2, \alpha_3 \in \{0, 1\}\}$. The crucial observation is that the coarse-grid correction operator K_h^H leaves the spaces of $2h$ -harmonics invariant for any arbitrary Fourier frequency $\boldsymbol{\theta}^{000} \in \widetilde{\Theta}_H = \Theta_H \setminus \Psi$, i. e.

$$K_h^H : \mathcal{F}^8(\boldsymbol{\theta}^{000}) \longrightarrow \mathcal{F}^8(\boldsymbol{\theta}^{000}).$$

This same invariance property is true for most of the smoothers considered here, i. e. $S_h : \mathcal{F}^8(\boldsymbol{\theta}^{000}) \longrightarrow \mathcal{F}^8(\boldsymbol{\theta}^{000})$. In particular, this is satisfied for line-type and plane-type relaxations used in next sections for poorly shaped tetrahedra, see [32, 34] for more details. Therefore, the two-grid operator $M_h^H = S_h^{\nu_2} K_h^H S_h^{\nu_1}$ also leaves the $2h$ -harmonic subspaces invariant. Hence, M_h^H is equivalent to a block-diagonal matrix consisting of 8×8 blocks denoted by $\widehat{M}_h^H(\boldsymbol{\theta}^{000}) = M_h^H|_{\mathcal{F}^8(\boldsymbol{\theta}^{000})}$,

with $\boldsymbol{\theta}^{000} \in \tilde{\Theta}_H$. For this reason, we can determine the spectral radius $\rho(M_h^H)$ by calculating the spectral radius of (8×8) -matrices

$$\rho(M_h^H) = \sup_{\boldsymbol{\theta}^{000} \in \tilde{\Theta}_H} \rho(\widehat{M}_h^H(\boldsymbol{\theta}^{000})). \quad (6)$$

In general, the suprema in (4) and (6) are computed numerically by sampling the Fourier space by an enough fine lattice. All the numerical results presented in this work have been performed by using a grid with mesh-size $1/32$ in the Fourier space, which provided accurate approximations of the corresponding factors.

The symbols corresponding to zebra-line and zebra-plane smoothers in tetrahedra grids are straightforwardly obtained from those in Cartesian coordinates. In fact some of them are identical and are presented in Appendix A2 in the LFA monograph of Wienands and Joppich [34].

3. Four color pattern relaxation

It is well-known that multicolor relaxations are very efficient smoothers for multigrid methods. They are constructed by splitting grid nodes into disjoint sets, with each set having a different color, and simultaneously updating all nodes of the same color. The best known example of this approach is the red-black Gauss–Seidel smoother for the five-point Laplace stencil. Such schemes have been extensively analyzed, see for example [23, 36, 37]. In this section we focus on the analysis of a four-color relaxation for discretizations on tetrahedral grids based on 15-point stencils. This smoother is defined in such a way all unknowns located at grid points with the same color can be updated simultaneously and independently of the unknowns associated with the other colors, an important property with regards to its parallelization. With this smoother, the two-grid operator does not leave the $2h$ -harmonic subspaces invariant, and therefore a more elaborate Fourier analysis is required.

3.1. Smoothing analysis

In this section we focus in the analysis of the four-color relaxation. The infinite grid G_h (1) is subdivided into four different type of grids G_h^i , $i = 0, 1, 2, 3$, each associated with a different color,

$$G_h^i = \{\mathbf{x} = (x_1, x_2, x_3) \mid x_j = k_j h_j, k_j \in \mathbf{Z}, j = 1, 2, 3, k_1 + k_2 + k_3 = i \pmod{4}\},$$

where (x_1, x_2, x_3) are the coordinates of the nodes of the grid in the basis $\{\mathbf{e}_1, \mathbf{e}_2, \mathbf{e}_3\}$. The special choice of this basis gives a different color to each vertex of a tetrahedron, in such way that the unknowns with the same color have no direct connection with each other, see Figure 2. More concretely,

for any grid point $\mathbf{x} = (x_1, x_2, x_3) \in G_h^i$ only the grid points of the form $(x_1 + \kappa_1 h_1, x_2 + \kappa_2 h_2, x_3 + \kappa_3 h_3)$, with

$$\begin{aligned} (\kappa_1, \kappa_2, \kappa_3) \in & \{(1, 0, 0), (1, 1, 0), (0, 1, 0), (-1, 0, 0), (-1, -1, 0), (0, -1, 0), \\ & (-1, 0, -1), (0, 0, -1), (-1, -1, -1), (0, -1, -1), \\ & (0, 0, 1), (1, 0, 1), (1, 1, 1), (0, 1, 1)\} \end{aligned}$$

contribute to the corresponding stencil (apart from \mathbf{x}). Note that none of these points belong to the grid G_h^i , i.e., $\kappa_1 + \kappa_2 + \kappa_3 \neq 0 \pmod{4}$. The four-color smoother is defined as a sequence of partial Jacobi sweeps in which the variables are updated, for example, in the order G_h^0, G_h^1, G_h^2 and G_h^3 . Notice that in each partial relaxation step, only the grid points of G_h^i are processed, whereas the remaining points are not treated. The smoothing operator $S_h^i(\omega_i)$ associated with the i^{th} -partial step is given by

$$S_h^i(\omega_i)v_h(\mathbf{x}) = \begin{cases} [(I_h - \omega_i D_h^{-1} L_h)v_h](\mathbf{x}), & \mathbf{x} \in G_h^i, \\ v_h(\mathbf{x}), & \mathbf{x} \in G_h \setminus G_h^i, \end{cases} \quad (7)$$

where D_h is the diagonal part of the discrete operator L_h and ω_i is a damping parameter related to the corresponding color. Therefore the complete four-color smoothing operator is given by the product of these four partial step operators, $S_h = S_h^3(\omega_3)S_h^2(\omega_2)S_h^1(\omega_1)S_h^0(\omega_0)$.

As the Fourier modes $\varphi_h(\boldsymbol{\theta}, \cdot)$ are not eigenfunctions of the smoothing operators $S_h^i(\omega_i), i = 0, \dots, 3$, a new strategy is necessary for the computation of the smoothing factor. For this, let us define the set of frequencies $\boldsymbol{\Lambda}_h$ given by

$$\boldsymbol{\Lambda}_h = \left(-\frac{\pi}{h_1}, \frac{\pi}{h_1}\right] \times \left(-\frac{\pi}{h_2}, \frac{\pi}{h_2}\right] \times \left(-\frac{\pi}{2h_3}, 0\right].$$

Given a frequency $\boldsymbol{\theta}_0 \in \boldsymbol{\Lambda}_h$, let us consider the four-dimensional subspace $\mathcal{F}^4(\boldsymbol{\theta}_0)$ given by

$$\mathcal{F}^4(\boldsymbol{\theta}_0) = \text{span}\{\varphi_h(\boldsymbol{\theta}_0, \cdot), \varphi_h(\boldsymbol{\theta}_1, \cdot), \varphi_h(\boldsymbol{\theta}_2, \cdot), \varphi_h(\boldsymbol{\theta}_3, \cdot)\}, \quad (8)$$

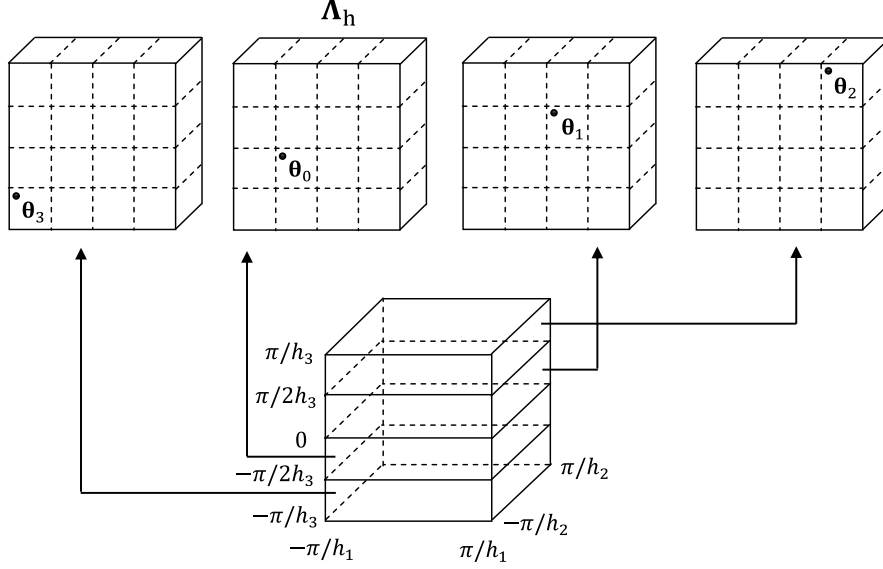
where $\boldsymbol{\theta}_\sigma = (\boldsymbol{\theta}_0 + \frac{\pi\sigma}{2}\mathbf{h}^{-1}) \pmod{2\pi\mathbf{h}^{-1}}$, $\sigma = 1, 2, 3$ and $\mathbf{h}^{-1} = (h_1^{-1}, h_2^{-1}, h_3^{-1})$. From the definition of $\boldsymbol{\theta}_\sigma$, it results that if $\boldsymbol{\theta}_0 \in \boldsymbol{\Lambda}_h$, each of the four coupled frequencies belongs to a different subregion of the frequency domain $\boldsymbol{\Theta}_h$, as observed in Figure 4. If $\boldsymbol{\theta}_0$ covers $\boldsymbol{\Lambda}_h$, the four frequencies defining the Fourier modes generating $\mathcal{F}^4(\boldsymbol{\theta}_0)$ fill the whole frequency domain $\boldsymbol{\Theta}_h$. Due to this fact, the Fourier space is given by the direct sum of subspaces $\mathcal{F}^4(\boldsymbol{\theta}_0)$, i.e.,

$$\mathcal{F}(G_h) = \bigoplus_{\boldsymbol{\theta}_0 \in \boldsymbol{\Lambda}_h} \mathcal{F}^4(\boldsymbol{\theta}_0).$$

We now show that for each $\boldsymbol{\theta}_0 \in \boldsymbol{\Lambda}_h$, the operators $S_h^i(\omega_i), i = 0, \dots, 3$ leave the spaces $\mathcal{F}^4(\boldsymbol{\theta}_0)$ invariant, i.e.,

$$S_h^i(\omega_i) : \mathcal{F}^4(\boldsymbol{\theta}_0) \rightarrow \mathcal{F}^4(\boldsymbol{\theta}_0), \quad i = 0, \dots, 3, \quad \boldsymbol{\theta}_0 \in \boldsymbol{\Lambda}_h.$$

Figure 4: Four-dimensional invariant harmonic subspaces for the four-color smoother



If operator $S_h^0(\omega_0)$ is applied to $\varphi_h(\boldsymbol{\theta}_0, \mathbf{x})$, we have that

$$S_h^0(\omega_0)\varphi_h(\boldsymbol{\theta}_0, \mathbf{x}) = \begin{cases} \lambda_0\varphi_h(\boldsymbol{\theta}_0, \mathbf{x}), & \mathbf{x} \in G_h^0, \\ \varphi_h(\boldsymbol{\theta}_0, \mathbf{x}), & \mathbf{x} \in G_h \setminus G_h^0, \end{cases} \quad (9)$$

where $\lambda_0 = 1 - \omega_0 \widehat{D}_h^{-1} \widehat{L}_h(\boldsymbol{\theta}_0)$ is the Fourier symbol of Jacobi relaxation, see [32], with \widehat{D}_h and $\widehat{L}_h(\boldsymbol{\theta}_0)$ the symbols of the operators D_h and L_h respectively. Expression (9) is not yet a Fourier representation of S_h^0 , however it is easy to see that $S_h^0(\omega_0)\varphi_h(\boldsymbol{\theta}_0, \mathbf{x}) \in \mathcal{F}^4(\boldsymbol{\theta}_0)$, i.e.,

$$S_h^0(\omega_0)\varphi_h(\boldsymbol{\theta}_0, \mathbf{x}) = \alpha_0(\boldsymbol{\theta}_0)\varphi_h(\boldsymbol{\theta}_0, \mathbf{x}) + \alpha_1(\boldsymbol{\theta}_0)\varphi_h(\boldsymbol{\theta}_1, \mathbf{x}) + \alpha_2(\boldsymbol{\theta}_0)\varphi_h(\boldsymbol{\theta}_2, \mathbf{x}) + \alpha_3(\boldsymbol{\theta}_0)\varphi_h(\boldsymbol{\theta}_3, \mathbf{x}) \quad (10)$$

with

$$\alpha_0(\boldsymbol{\theta}_0) = \frac{\lambda_0 + 3}{4}, \quad \alpha_1(\boldsymbol{\theta}_0) = \alpha_2(\boldsymbol{\theta}_0) = \alpha_3(\boldsymbol{\theta}_0) = \frac{\lambda_0 - 1}{4}.$$

These coefficients are obtained by evaluating expressions (9) and (10) in the four subgrids $G_h^i, i = 0, \dots, 3$:

$$\begin{aligned} \alpha_0(\boldsymbol{\theta}_0) + \alpha_1(\boldsymbol{\theta}_0) + \alpha_2(\boldsymbol{\theta}_0) + \alpha_3(\boldsymbol{\theta}_0) &= \lambda_0, & \text{if } \mathbf{x} \in G_h^0, \\ \alpha_0(\boldsymbol{\theta}_0) + e^{i\pi/2}a_1(\boldsymbol{\theta}_0) + e^{i\pi}a_2(\boldsymbol{\theta}_0) + e^{i3\pi/2}a_3(\boldsymbol{\theta}_0) &= 1, & \text{if } \mathbf{x} \in G_h^1, \\ \alpha_0(\boldsymbol{\theta}_0) + e^{i\pi}a_1(\boldsymbol{\theta}_0) + e^{i2\pi}a_2(\boldsymbol{\theta}_0) + e^{i3\pi}a_3(\boldsymbol{\theta}_0) &= 1, & \text{if } \mathbf{x} \in G_h^2, \\ \alpha_0(\boldsymbol{\theta}_0) + e^{i3\pi/2}a_1(\boldsymbol{\theta}_0) + e^{i3\pi}a_2(\boldsymbol{\theta}_0) + e^{i9\pi/2}a_3(\boldsymbol{\theta}_0) &= 1, & \text{if } \mathbf{x} \in G_h^3, \end{aligned}$$

and solving the corresponding 4×4 -system. Analogously, if we denote by

$$S_h^0(\omega_0)\varphi_h(\boldsymbol{\theta}_\sigma, \mathbf{x}) = \begin{cases} \lambda_\sigma \varphi_h(\boldsymbol{\theta}_\sigma, \mathbf{x}), & \mathbf{x} \in G_h^0, \\ \varphi_h(\boldsymbol{\theta}_\sigma, \mathbf{x}), & \mathbf{x} \in G_h \setminus G_h^0, \end{cases} \quad (11)$$

where $\lambda_\sigma = 1 - \omega_\sigma \widehat{D}_h^{-1} \widehat{L}_h(\boldsymbol{\theta}_\sigma)$ for $\sigma = 1, 2, 3$, we can write

$$S_h^0(\omega_0)\varphi_h(\boldsymbol{\theta}_\sigma, \mathbf{x}) = \alpha_0(\boldsymbol{\theta}_\sigma)\varphi_h(\boldsymbol{\theta}_0, \mathbf{x}) + \alpha_1(\boldsymbol{\theta}_\sigma)\varphi_h(\boldsymbol{\theta}_1, \mathbf{x}) + \alpha_2(\boldsymbol{\theta}_\sigma)\varphi_h(\boldsymbol{\theta}_2, \mathbf{x}) + \alpha_3(\boldsymbol{\theta}_\sigma)\varphi_h(\boldsymbol{\theta}_3, \mathbf{x}), \quad \sigma = 1, 2, 3, \quad (12)$$

with

$$\alpha_{\sigma'}(\boldsymbol{\theta}_\sigma) = \begin{cases} \frac{\lambda_\sigma + 3}{4}, & \text{if } \sigma' = \sigma, \\ \frac{\lambda_\sigma - 1}{4}, & \text{otherwise.} \end{cases}$$

We conclude that for each $\boldsymbol{\theta}_0 \in \boldsymbol{\Lambda}_h$, the operator $S_h^0(\omega_0)$ leaves the space $\mathcal{F}^4(\boldsymbol{\theta}_0)$ invariant, and its matrix representation is the (4×4) -matrix

$$\widehat{S}_h^0(\boldsymbol{\theta}_0) = \frac{1}{4} \begin{pmatrix} \lambda_0 + 3 & \lambda_1 - 1 & \lambda_2 - 1 & \lambda_3 - 1 \\ \lambda_0 - 1 & \lambda_1 + 3 & \lambda_2 - 1 & \lambda_3 - 1 \\ \lambda_0 - 1 & \lambda_1 - 1 & \lambda_2 + 3 & \lambda_3 - 1 \\ \lambda_0 - 1 & \lambda_1 - 1 & \lambda_2 - 1 & \lambda_3 + 3 \end{pmatrix}. \quad (13)$$

Analogously, the (4×4) -matrices $\widehat{S}_h^1(\boldsymbol{\theta}_0)$, $\widehat{S}_h^2(\boldsymbol{\theta}_0)$, $\widehat{S}_h^3(\boldsymbol{\theta}_0)$ associated with the smoothing operators $S_h^1(\omega_1)$, $S_h^2(\omega_2)$ and $S_h^3(\omega_3)$ can be determined, yielding to the following expressions:

$$\widehat{S}_h^1(\boldsymbol{\theta}_0) = \frac{1}{4} \begin{pmatrix} \lambda_0 + 3 & i(\lambda_1 - 1) & 1 - \lambda_2 & i(1 - \lambda_3) \\ i(1 - \lambda_0) & \lambda_1 + 3 & i(\lambda_2 - 1) & 1 - \lambda_3 \\ 1 - \lambda_0 & i(1 - \lambda_1) & \lambda_2 + 3 & i(\lambda_3 - 1) \\ i(\lambda_0 - 1) & 1 - \lambda_1 & i(1 - \lambda_2) & \lambda_3 + 3 \end{pmatrix}, \quad (14)$$

$$\widehat{S}_h^2(\boldsymbol{\theta}_0) = \frac{1}{4} \begin{pmatrix} \lambda_0 + 3 & 1 - \lambda_1 & \lambda_2 - 1 & 1 - \lambda_3 \\ 1 - \lambda_0 & \lambda_1 + 3 & 1 - \lambda_2 & \lambda_3 - 1 \\ \lambda_0 - 1 & 1 - \lambda_1 & \lambda_2 + 3 & 1 - \lambda_3 \\ 1 - \lambda_0 & \lambda_1 - 1 & 1 - \lambda_2 & \lambda_3 + 3 \end{pmatrix}, \quad (15)$$

$$\widehat{S}_h^3(\boldsymbol{\theta}_0) = \frac{1}{4} \begin{pmatrix} \lambda_0 + 3 & i(1 - \lambda_1) & 1 - \lambda_2 & i(\lambda_3 - 1) \\ i(\lambda_0 - 1) & \lambda_1 + 3 & i(1 - \lambda_2) & 1 - \lambda_3 \\ 1 - \lambda_0 & i(\lambda_1 - 1) & \lambda_2 + 3 & i(1 - \lambda_3) \\ i(1 - \lambda_0) & 1 - \lambda_1 & i(\lambda_2 - 1) & \lambda_3 + 3 \end{pmatrix}. \quad (16)$$

Finally, we have that $\widehat{S}_h(\boldsymbol{\theta}_0) = \widehat{S}_h^3(\boldsymbol{\theta}_0)\widehat{S}_h^2(\boldsymbol{\theta}_0)\widehat{S}_h^1(\boldsymbol{\theta}_0)\widehat{S}_h^0(\boldsymbol{\theta}_0)$ is the (4×4) -matrix representation of S_h in $\mathcal{F}^4(\boldsymbol{\theta}_0)$ and the smoothing factor per sweep, for ν consecutive sweeps, is given by

$$\mu(S_h, \nu) = \sup_{\boldsymbol{\theta}_0 \in \boldsymbol{\Lambda}_h} \sqrt[\nu]{\rho(\widehat{Q}(\boldsymbol{\theta}_0)\widehat{S}_h^\nu(\boldsymbol{\theta}_0))}, \quad (17)$$

where $\widehat{Q}(\boldsymbol{\theta}_0) = \text{diag}(q(\boldsymbol{\theta}_0), q(\boldsymbol{\theta}_1), q(\boldsymbol{\theta}_2), q(\boldsymbol{\theta}_3))$ is a diagonal matrix with

$$q(\boldsymbol{\theta}_\sigma) = \begin{cases} 0, & \text{if } \boldsymbol{\theta}_\sigma \in \Theta_H, \\ 1, & \text{otherwise,} \end{cases}$$

for $\sigma = 0, \dots, 3$. Notice that the projection matrix $\widehat{Q}(\boldsymbol{\theta}_0)$ annihilates the low-frequency error components and leaves the high-frequency error components unchanged.

3.2. Two-grid analysis

The smoothing factor give by formula 17 should accurately approximate the actual multigrid convergence, if the considered multigrid coarse-grid correction is close to the idealized coarse-grid correction. In other case, a two-grid analysis is necessary to understand the interplay between the smoothing and the coarse-grid correction process. To perform a two-grid analysis, Fourier space $\mathcal{F}(G_h)$ is divided into a direct sum of sixteen-dimensional subspaces $\mathcal{F}(G_h) = \oplus \mathcal{F}^{16}(\boldsymbol{\theta}_0^{000})$, where $\boldsymbol{\theta}_0^{000} \in \Lambda_H$, with

$$\Lambda_H = \left(-\frac{\pi}{2h_1}, \frac{\pi}{2h_1} \right] \times \left(-\frac{\pi}{2h_2}, \frac{\pi}{2h_2} \right] \times \left(-\frac{\pi}{2h_3}, 0 \right].$$

These sixteen-dimensional subspaces are defined as

$$\mathcal{F}^{16}(\boldsymbol{\theta}_0^{000}) = \mathcal{F}^4(\boldsymbol{\theta}_0^{000}) \oplus \mathcal{F}^4(\boldsymbol{\theta}_0^{110}) \oplus \mathcal{F}^4(\boldsymbol{\theta}_0^{100}) \oplus \mathcal{F}^4(\boldsymbol{\theta}_0^{010}),$$

where $\boldsymbol{\theta}_0^{110}, \boldsymbol{\theta}_0^{100}, \boldsymbol{\theta}_0^{010}$ are the three frequencies associated with $\boldsymbol{\theta}_0^{000}$ by means of (5) and the subspace $\mathcal{F}^4(\boldsymbol{\theta}_0^{ij0})$ is generated as in (8).

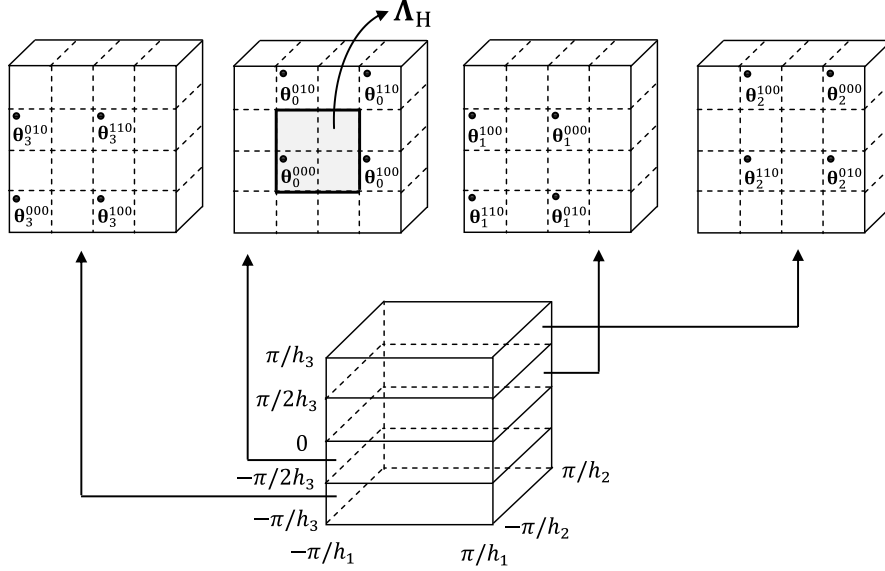
Figure 5 illustrates the location of the sixteen different frequencies $\boldsymbol{\theta}_\sigma^{ij0}$ and the region Λ_H . From the invariance results of the previous sections, it can be observed that the subspaces $\mathcal{F}^{16}(\boldsymbol{\theta}_0^{000})$ are invariant for both the four-color smoother and the standard coarsening operator. Notice that in each subspace $\mathcal{F}^{16}(\boldsymbol{\theta}_0^{000})$, we can find associated two low-frequencies $\boldsymbol{\theta}_0^{000}$ and $\boldsymbol{\theta}_1^{000}$, and their seven corresponding high-frequency harmonics. Therefore, if $\boldsymbol{\theta}_0^{000}$ covers the whole Λ_H then two coupled low-frequencies fill the subset Θ_H of low frequencies. This fact together with the coupling of a low-frequency with seven high frequency modes implies that the sixteen frequencies defining the Fourier modes generating $\mathcal{F}^{16}(\boldsymbol{\theta}_0^{000})$ fill the whole frequency domain Θ_h .

The matrix representation of $S_h^i(\omega_i)$ in $\mathcal{F}^{16}(\boldsymbol{\theta}_0^{000})$, $\boldsymbol{\theta}_0^{000} \in \Lambda_H$, is now the (16×16) -block matrix $\text{diag}[\widehat{S}_h^i(\boldsymbol{\theta}_0^{000}), \widehat{S}_h^i(\boldsymbol{\theta}_0^{110}), \widehat{S}_h^i(\boldsymbol{\theta}_0^{100}), \widehat{S}_h^i(\boldsymbol{\theta}_0^{010})]$, where the 4×4 diagonal matrices $\widehat{S}_h^i(\boldsymbol{\theta}_0^{ij0})$ are given in (13)-(16). The matrix representation $\widehat{K}_h^H(\boldsymbol{\theta}_0^{000})$ of the coarse-grid correction operator K_h^H in $\mathcal{F}^{16}(\boldsymbol{\theta}_0^{000})$ is a (16×16) -block matrix, constructed in the usual way from the two low-frequencies $\boldsymbol{\theta}_0^{000}$ and $\boldsymbol{\theta}_1^{000}$ defining the two smooth Fourier modes in $\mathcal{F}^{16}(\boldsymbol{\theta}_0^{000})$.

The definition of the asymptotic convergence factor for a two-grid cycle with ν_1 pre-smoothing and ν_2 post-smoothing steps now becomes

$$\rho(M_h^H) = \sup_{\boldsymbol{\theta}_0^{000} \in \Lambda_H} \rho(\widehat{M}_h^H(\boldsymbol{\theta}_0^{000})) = \sup_{\boldsymbol{\theta}_0^{000} \in \Lambda_H} \rho(\widehat{S}_h^{\nu_2}(\boldsymbol{\theta}_0^{000}) \widehat{K}_h^H(\boldsymbol{\theta}_0^{000}) \widehat{S}_h^{\nu_1}(\boldsymbol{\theta}_0^{000})), \quad (18)$$

Figure 5: Sixteen-dimensional minimal invariant harmonic subspaces for the four-color smoother



with

$$\tilde{\Lambda}_H = \Lambda_H \setminus \{\theta_0^{000} \in \Lambda_H \mid \widehat{L}_H(2\theta_\sigma^{jkl}) = 0, \text{ or } \widehat{L}_h(\theta_\sigma^{jkl}) = 0, \sigma = 0, 1, 2, 3, j, k, l \in \{0, 1\}\}.$$

4. Fourier analysis results

This section is devoted to show some LFA results in order to design efficient multigrid methods for different shapes of tetrahedra. We mainly focus on the choice of good smoothers for poorly shaped tetrahedra which are inevitably produced by commonly used mesh generators.

In order to compare the convergence factors predicted by LFA, a W-cycle is used since a two-grid cycle is often not practical since it would require a high computational effort on the coarse grid. However, the convergence factors are similar to a two-grid cycle. The LFA assumes an infinitely large regular domain. In practice, such a domain can be approximated by a regular grid with a very large number of unknowns. In experiments, structured meshes of $2.1 \cdot 10^6$ elements (129 grid points in each direction) easily turned out to be sufficient to exhibit the asymptotic behaviour. Similar number of grid points in each directions are necessary in 2D. In the experiment, the solution is initialized with random values between -1.0 and 1.0 . The errors for determining the convergence rates are measured with the discrete L2 norm, using the observed

rate of error reduction in the 151st cycle as approximation to the asymptotic value.

If not stated differently, all relaxation parameters are found by LFA for the remaining paper. At first we are interested to find optimal relaxation parameters w.r.t. the convergence rate. To cover the complete search space, all different relaxation parameters up to $\omega = 2.0$ are predicted with a resolution $d\omega = 0.05$ for each different color and the best is chosen. In section 5.3.3, a downhill simplex method [27] is used that turned out to be stable and additionally much more computationally efficient. Both methods were compared and achieved very similar convergence rates.

4.1. Regular tetrahedron

We first turn our attention to the ω -Jacobi, the lexicographic Gauss-Seidel and the four-color smoother for a regular tetrahedron, that is characterized by having edges of equal length. In the case of Jacobi relaxation, we use the optimal parameter $\omega = 0.8$ as predicted by LFA. For the Gauss-Seidel and 4-color smoothers no damping is applied. In Table 1 we show for different pre-smoothing (ν_1) and post-smoothing (ν_2) steps the smoothing factor μ , the two-grid convergence factor ρ as predicted by LFA, and the experimental observed convergence factor obtained by using W -cycles. Clearly the two-grid convergence factors are very well predicted by LFA in all cases. We also observe that the four-color smoother provides the best convergence factors among the considered point-wise smoothers.

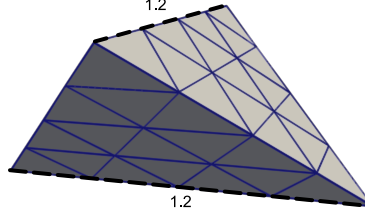
It should be noted that the smoothing factors on tetrahedra are somewhat worse than one would expect for triangles in 2D. For example, the smoothing factor of Gauss-Seidel on an equilateral triangle is 0.416 in 2D, while it is 0.521 for a regular tetrahedron in 3D. This behaviour is similar to what is observed for standard finite difference discretizations of the 3D Poisson equation (see, for example [32]).

In passing, note that it is possible to improve the convergence factors of the four-color smoother by using relaxation parameters. For instance, in the case of $(\nu_1, \nu_2) = (2, 1)$, the convergence factor for four-color smoother can be improved from 0.153 to 0.090 by using overrelaxation parameters $\omega_i = 1.15, 1.20, 1.25, 1.25$ as introduced in (7). Similarly for lexicographic Gauss-Seidel, the convergence factor can be improved from 0.176 to 0.141 with the relaxation parameter $\omega = 1.2$.

4.2. Optimized tetrahedron

A regular input tetrahedron is not the best shape for our regular refinement with respect to the convergence rate. Inside a structured region of a refined coarse grid element, one pair of stencil entries relates to an edge of the element. After one refinement step, four child elements are similar to the parent element, only translated and scaled by the factor 0.5. The remaining four child elements contain six edges of its parent element, which are translated and scaled by the factor 0.5. The remaining seventh edge is introduced by Bey's refinement [5].

Figure 6: Optimized tetrahedron with two non-unit edge lengths



This edge is located between the midpoint of edge e_{02} and the midpoint of edge e_{13} (see Figure 3) of the parent element. The subscripts denote the vertex indices of the refined element. In the case of a regular tetrahedron, all edges except of the additional introduced edge have the same length. In contrast to the six other entry pairs, which are typically negative, the seventh pair has positive entries in the stencil. Thus, compared to the other edges there is a weak connection, if this edge is small. For example by setting the edge lengths of e_{02} and e_{13} equal to 1.2 and keeping all other four edge sizes equal to 1.0, we receive an optimized tetrahedron concerning the convergence rate (see Figure 6).

The exceptional convergence factors associated with the four-color smoother for this optimized tetrahedron are pointed out in Table 2. On this type of tetrahedra, the convergence factor of the four-color smoother is approximately $\rho = 0.106$ for one pre- and post-smoothing steps, having at the same time the desirable property of high parallelism. This factor can also be further enhanced to 0.080 using damping parameters of values $\omega = (1, 1, 1, 1.2)$.

ν_1, ν_2	Damped Jacobi			Gauss-Seidel			Four-color		
	$\mu^{\nu_1+\nu_2}$	ρ	ρ_h	$\mu^{\nu_1+\nu_2}$	ρ	ρ_h	$\mu^{\nu_1+\nu_2}$	ρ	ρ_h
1, 0	0.741	0.640	0.637	0.521	0.434	0.427	0.500	0.407	0.389
1, 1	0.550	0.409	0.407	0.272	0.223	0.219	0.250	0.195	0.197
2, 1	0.406	0.298	0.297	0.141	0.176	0.174	0.125	0.153	0.153
2, 2	0.301	0.250	0.250	0.074	0.143	0.141	0.062	0.123	0.125

Table 1: LFA smoothing factors, $\mu^{\nu_1+\nu_2}$, LFA two-grid convergence factors, ρ , and measured W -cycle convergence rates, ρ_h , for a regular tetrahedron

ν_1, ν_2	Damped Jacobi			Gauss-Seidel			Four-color		
	$\mu^{\nu_1+\nu_2}$	ρ	ρ_h	$\mu^{\nu_1+\nu_2}$	ρ	ρ_h	$\mu^{\nu_1+\nu_2}$	ρ	ρ_h
1, 0	0.720	0.602	0.598	0.492	0.401	0.392	0.442	0.345	0.331
1, 1	0.517	0.362	0.360	0.243	0.151	0.145	0.196	0.106	0.105

Table 2: LFA smoothing factors, $\mu^{\nu_1+\nu_2}$, LFA two-grid convergence factors, ρ , and measured W -cycle convergence rates, ρ_h , for an optimized tetrahedron

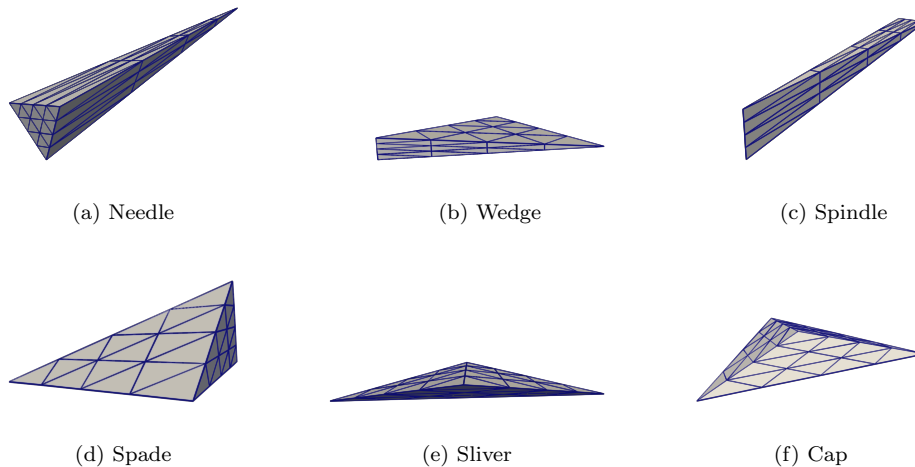


Figure 7: Different classes of degenerated elements

4.3. Degenerated tetrahedra

On the other hand, the highly satisfactory convergence factors obtained for regular and optimized tetrahedra, can deteriorate quickly when poorly shaped tetrahedra are treated. In two dimensions, there are only two types of failure, angles close to 0° and angles close to 180° , and no failures of the first kind implies no failures of the second. In three dimensions, we can classify poorly shaped tetrahedra according to both dihedral and solid angles. Dihedral is the interior angle between two face planes, while solid angles are formed by the intersection of three planes at one vertex. There are then six types of bad tetrahedra, as shown in Figure 7.

Table 3 shows the characteristics of differently shaped tetrahedra. Besides the number of solid and dihedral angles, the edge ratio, minimal and maximal angles between two edges are provided for an exemplary tetrahedron of this type. For these elements, the smoothing factor and the two-grid convergence factor are given for one pre- and one post-smoothing step ($\nu_1 = 1, \nu_2 = 1$). Poor behavior of the four-color smoother for these type of tetrahedra is shown together with the good performance that is observed for the regular and optimized tetrahedra.

4.3.1. Wedge

To overcome this difficulty, we propose specific smoothers for some of the poorly shaped tetrahedra. The first type of such tetrahedra is the wedge type, which has one edge much smaller than the others. This causes two entries of the stencil to be much larger than the others, producing the strongest connection in one direction. Since the common lore states that the good smoothing of errors is obtained when the strongly coupled unknowns are collectively relaxed, a line smoothing in the direction of the smaller edge is expected to improve the

	Regular	Optimized	Needle	Wedge	Spindle	Spade	Sliver	Cap
Small solids	-	-	1	-	-	-	-	-
Large solids	-	-	-	2	-	1	-	1
Small dihedrals	-	-	-	1	2	2	4	3
Large dihedrals	-	-	-	-	-	1	2	3
$\mu^{\nu_1+\nu_2}$	0.250	0.196	0.982	0.786	0.980	0.590	0.896	0.872
ρ	0.195	0.106	0.982	0.740	0.980	0.500	0.889	0.739
Edge ratio	1.0	1.15	10.0	4.0	10.0	1.67	1.40	1.71
Min angle	60 ⁰	54.9 ⁰	5.7 ⁰	14.3 ⁰	5.7 ⁰	33.6 ⁰	45.6 ⁰	31.4 ⁰
Max angle	60 ⁰	70.2 ⁰	87.1 ⁰	82.8 ⁰	87.1 ⁰	112.9 ⁰	88.9 ⁰	117.2 ⁰

Table 3: LFA smoothing factors, $\mu^{\nu_1+\nu_2}$, and two-grid convergence factors, ρ , of the four-color smoother for different tetrahedra

performance. In fact, a two-grid convergence factor 0.122 is obtained by using the corresponding line smoother with one pre- and one post-smoothing steps. For very anisotropic wedge-type tetrahedra improved convergence rate easily compensated the somewhat higher computational cost of the tridiagonal solvers in the line smoother. Table 4 presents an overview of the effect of line-wise and plane-wise smoothers onto the convergence rate for this and the following tetrahedral shapes.

	Wedge	Spade	Needle	Spindle	Sliver/Cap
Line-wise	good	middle	poor	poor	poor
Plane-wise	good	good	good	good	poor

Table 4: Smoothing properties of line-wise and plane-wise smoothers for different tetrahedra

4.3.2. Spade

Another tetrahedral shape is generated by assuming two short edges, which are connected to each other. Keeping the other edge lengths similar but larger results in a spade. In comparison to the needle-type, discussed next, only two stencil-pairs of three in a plane are large. Already an improvement is visible, choosing a line-wise smoothing in the direction of one short edge. With two smoothing steps in total, the computational work is comparable to point-wise smoothing, but results in a better convergence rate of 0.23. Hereby it yields to similar convergence, regardless of smoothing alternatively in both directions of the short edges, or repeatedly along one of them. Point-wise smoothing only provides a convergence rate of 0.59 (see Table 3).

Another possibility is applying a zebra-plane smoothing about the faces spanned by those edges. With only one smoothing step, a plane-zebra smoother yields convergence factors about 0.105. Whether or not this reduces the overall cost depends on the implementation of the plane-smoother and the degree of anisotropy. Indeed, because of significant higher costs of plane-wise smoothing in our current implementation, discussed in the next section, we would choose line-wise smoothing for that example.

4.3.3. *Needle*

The next bad tetrahedron is the needle-type, which is characterized by the fact that one vertex is far away from the opposing face. This feature produces a stencil with stronger connections in the direction of the plane defined by the face opposite to such vertex. Therefore, the corresponding plane relaxation will result in excellent smoothing. In fact, a very good convergence factor about 0.121 is reached with only one smoothing step for a zebra-plane smoother. We want to emphasize the fact of the use of zebra-plane smoothers rather than lexicographic plane relaxation. This is due to the significant improvement of the convergence factors when zebra-type smoothers are used. For example, in this case a factor of 0.330 is provided by lexicographic plane relaxation. Thus one plane-zebra sweep is roughly as effective as two lexicographic plane sweeps ($(0.330)^2 = 0.1089$). One might think that alternating line relaxation with respect to the two directions defining the corresponding face could be a suitable choice, but very poor convergence factors are provided by this strategy. For instance, only a factor of about 0.942 is obtained when using two smoothing steps. We remark that all strongly connected unknowns should be relaxed collectively and therefore a plane smoother must be used.

4.3.4. *Spindle*

Analogously, the behavior of the spindle-type is similar to that of needle type. In this case the strong connection also corresponds to the direction of a face of the tetrahedron, and therefore a plane smoothing will be a good choice. Again, very satisfactory convergence properties are provided by using such smoother. LFA predicts a two-grid convergence factor about 0.124 with only one smoothing step if the adequate zebra-plane smoother is activated, that is, the zebra-plane relaxation updating all strongly connected unknowns.

4.3.5. *Sliver and cap*

According to Shewchuk [30] "good" tetrahedra are of two types: those that are not flat, and those that can grow arbitrarily flat without having a large planar or dihedral angle. The "bad" tetrahedra result in error bounds that explode, and a dihedral angle or a planar angle that approaches 180^0 , as they are flattened. Sliver as well as cap type can grow arbitrary flat and have in addition large planar or dihedral angles and thus have bad interpolation properties.

For a different reason, we also were not able to find an optimal collective relaxation method for sliver and cap type. Here, the strongly connected points are not located on an edge or plane; therefore the smallest block would already include all grid points. In principle alternating plane relaxations, or alternating line relaxations improve the convergence rate compared to a point-wise relaxation like shown for a spade. However, similarly in this case the convergence rate deteriorates when the degree of anisotropy increases.

However, this is not a limitation from the practical point of view. Many Delaunay mesh generators include a post-processing to find and remove sliver and cap type tetrahedra, because of the poor approximation quality of the finite element methods using these types.

5. Numerical experiments

In this section we will discuss numerical experiments to illustrate two different strategies, from subsection 5.2 and 5.3. Firstly, we will demonstrate how to use LFA to design efficient multigrid solvers for semi-structured tetrahedral grids. We will use the block-wise processing to choose different smoothers depending on the shape of the tetrahedra. This kind of strategy has already been used successfully for two-dimensional linear-elasticity problems in [14]. Here, we will apply it for three-dimensional tetrahedral meshes. The second strategy consists of applying LFA to improve the overall convergence rates by adapting smoothing parameters. This include the damping parameters, number of pre- and post-smoothing steps, and smoother types individually for each block, in a complex domain.

5.1. Computational cost for our implementation

Especially for the more sophisticated smoothers it is important to keep their computational costs in mind. The computational costs of an algorithm is often expressed in arithmetic operations. An advantage of this measure is its platform independence. Unfortunately, it often cannot give realistic predictions of performance for an implementation on specific hardware. The runtime on many modern architectures is dictated by memory bandwidth, cache effects, instruction level parallel execution, or memory alignment issues. Here we will present an overview of the smoothers that are available in HHG. To allow a fair comparison, all algorithms are implemented in an efficient way, but are not yet optimized specifically for each architecture. The performance is evaluated on one core of a *Xeon 5550 Nehalem* chip with 8 MB shared cache per chip. The code was produced by the *Intel 10.1* compiler (*flags: -O3*). We will measure the required number of clock cycles per unknown for three different block sizes for a structured region: 65, 129 and 257 unknowns in each direction (see Table 5). Most differences can be attributed to cache-effects. Applying damping parameters cost additional 3 clock cycles or less. This is not really severe for any of the schemes introduced. Thus it should be applied, if it leads to advantages.

The compiler is basically able to utilize SSE SIMD instructions (small vector processing) for the stencil evaluations. For large vectors, a 4-color smoother with a splitting of the colors to different arrays would be necessary to achieve a good performance. Further, the data layout on the structured regions would also fit well to a parallel execution on GPUs. Here, especially smoothers with a low degree of dependency (like a 4-color smoother, zebra-line smoother, or a parallel plane-wise smoother) would be most suitable.

Especially to perform line-wise or plane-wise smoothing over interface boundaries, using a multigrid in one or two dimensions seems to be a promising approach. However it not always obvious to define a line or plane for the whole domain, since the coarsest mesh is unstructured.

Line-wise smoother. The line-wise smoother is implemented by the Thomas' Algorithm or tridiagonal matrix algorithm, a simplified version of Gaussian

elimination. For constant coefficients, terms involving only the coefficients of the stencil are calculated once per stencil. Thus the required operations per unknown are comparable to a Gauss-Seidel smoothing. The number of clock cycles is only slightly higher. A zebra-line fashion has a high degree of parallelism in two directions. A parallel execution in the line-wise direction can be achieved by cyclic reduction (see e.g. [21]).

Plane-wise smoother. The advantage of an iterative method for a plane-wise smoother is that the plane does not have to be solved exactly. A good approximation is enough to obtain an optimal convergence rate of the whole V-cycle. This behavior was observed e.g. in [25], where a 2-dimensional multigrid is used for each plane.

For tetrahedral structured regions, it is not straightforward to apply plane-wise multigrid, since each plane size has a different size. Therefore, we solved arising system by a Conjugate Gradient (CG) algorithm. Since the number of CG iterations increases with respect to a growing plane-size, also the number arithmetic operations and thus solving time are effected.

Algorithm	Operations	Clock cycles (line sizes)		
		65	129	257
lex. Gauss-Seidel	29	35	35	36
Four-color	29	40	39	40
Line-wise	29	40	39	41
Plane-wise	270-600	360	456	694

Table 5: Arithmetic costs per unknown and measured clock cycles for a Gauss-Seidel, four-color, line-wise and plane-wise smoothers

5.2. Smoothers on semi-structured meshes

In the previous section we presented the impact of strongly anisotropic meshes on the convergence rate for structured tetrahedral meshes. Furthermore we found appropriate line- and plane-smoothing strategies for different types of element degeneration. In a smoothing step of HHG, we first smooth the the interface points (macro vertices, edges, and faces) between all structured regions. Afterward we smooth the structured regions themselves. While for point-wise smoothing this proceeding has nearly no influence on the convergence [22], we will study its influence for plane- or line-smoothing in the first numerical experiment, where we measure the impact of the interface points between the structured regions using semi-structured meshes. In the second subsection, the advantages of using different smoothers for different shaped tetrahedra composing the domain are displayed.

5.2.1. Anisotropic smoothing

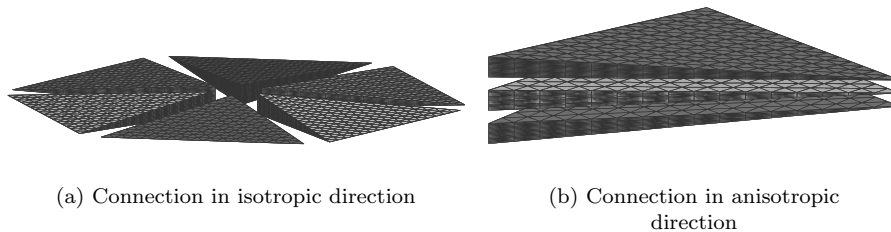
In the following two numerical experiments we construct our computational domain out of the wedge type elements. Figure 8 (a) shows a setup where six

structured regions are sharing anisotropic faces. In Figure 8 (b) the same type of tetrahedra are used, but are here connected at their regular triangular face. In the following part, we apply two smoothing steps for all smoothers. The convergence factors are measured after 50 W-cycles. We point out that the used elements have a edge ratio of 10 between the shortest and the largest edge length and dihedral angles of 5.7° . Otherwise the following discussed effects are not so severe. On the fine grid we end up with $1.73 \cdot 10^7$ elements in case (a) and $3.46 \cdot 10^7$ elements in case (b).

For a single region, lexicographic Gauss-Seidel achieves a convergence factor of 0.934. This factor is nearly the same for both domains (a) and (b). In contrast a line smoother yields a convergence factor of 0.072 for a single region. For domain (a) the interfaces slightly effect the convergence rate to 0.094. However it is worse if we cannot solve the full line of unknowns along the strong coupling, but only parts of the line. This is case for domain (b) since two interfaces are breaking these lines and do not allow a fully collective line-smoothing. This explains a bad convergence factor of 0.847 for (b). Damping parameter of 1.05 inside the structured regions and 1.15 for the boundary points help a bit to decrease the convergence factor to 0.796. This problem has been reported in some papers about grid-partitioning, see for example [28]. If possible, this case should be avoided in the original partitioning of the domain.

The same behavior is observed by applying plane smoothing to adjoined needle or spindle type regions. In these cases lines of unknowns, which are not collectively updated since they are interface points, increase the convergence rate.

Figure 8: Connecting faces in different directions



5.2.2. Locally adaptive smoothing

Contrary to the previous examples, we apply different smoothers according to the geometry of the structured region. A model domain consisting of four different tetrahedral types is presented in Figure 9. Wedge and needle elements share some of their faces with regular elements. The whole domain consists of $1.73 \cdot 10^7$ tetrahedron elements on the finest level. Table 6 shows some properties of the single structured regions without its interfaces to any other regions.

Figure 9: Domain consisting of wedge, regular and needle tetrahedral types



In order to get a similar convergence rate for the composed domain, we choose different smoothers according to the underlying mesh geometry. The regular tetrahedra are smoothed by using four-color relaxation with damping parameters $\omega = (1.15, 1.20, 1.25, 1.25)$, and two pre- and one post-smoothing steps. From Section 4, we know that a convergence factor of about 0.09 is achieved for these regular tetrahedra. For the wedge element, again a value of 0.09 is predicted by LFA, if a line-smoother is used with two pre- and one-smoothing steps. By the other hand, for the needle tetrahedron a zebra-plane smoother with only one smoothing step is enough to reach a convergence factor about 0.12. Taking into account these local convergence factors and considering the worst of them, we can predict a global factor of 0.12 for the composed domain.

By performing the multigrid algorithm with the corresponding local components chosen above, a convergence factor of 0.17 is obtained for the whole computational domain. An additional smoothing step of the macro faces after smoothing the interior was applied. Using damping parameter at the interface points and in the structured regions, the convergence factor improves to 0.14, which is very close to the expected value of 0.12. As a reference, a standard lexicographic Gauss-Seidel with $\nu_1, \nu_2 = 2, 1$ provides a convergence factor of 0.95. It turns out that using different smoothing strategies depending on the sub-domains is very advantageous and following this rule, very efficient multigrid solvers can be designed for quite complicated three-dimensional domains. However to be fair, one has to consider the additional computational overhead for line- or plane-smoothing. If and how much it pays out can also depend much on the implementation of the smoothers.

Shape	edge ratio	max angle	min angle	smoothing	ν_1, ν_2	ρ
Needle	10	87°	5.7°	plane-wise	1,0	0.12
Regular	1	60°	60°	4-color	2,1	0.09
Wedge	5	110°	11°	line-wise	2,1	0.09

Table 6: Convergence factor for the single structured regions

5.3. Locally adaptive damping and smoothing steps on semi-structured meshes

In order to achieve a good overall convergence of the solver, we try to distribute the computational work such that all regions of the domain receive a similar error reduction in each smoothing step. In our approach we use LFA to

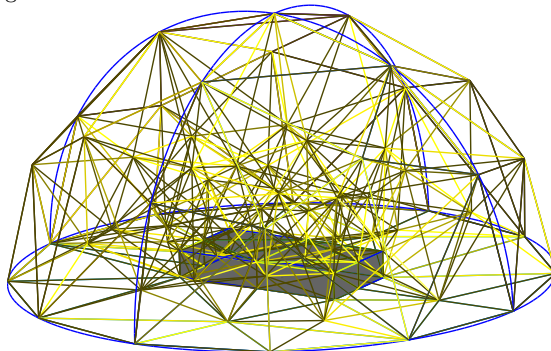
control this process. Partial smoothing has already been promoted, e. g., in [8]. In addition to that, we apply individual damping parameters to each structured region.

With HHG’s semi-structured meshes it is relatively easy to locally adapt smoothing parameters to mesh-induced convergence rate variations. Since each coarse mesh element gets refined in a regular way (cf. Fig. 1), all its sub-elements are similar, and the operator stencils of all interior grid points are the same. Therefore, one can determine the optimal smoothing parameters for each coarse grid element and use them for all its sub-elements. We will use LFA prediction to optimize the convergence rate of the structured regions by choosing suitable the smoother parameters. Further we will provide suggestions how to deal with interface points between those regions. Step by step we will apply different modifications to the smoothing procedure and observe its influence. Thus we end up with an asynchronous or chaotic smoothing [1, 2, 11]. However, this is usually a result of an efficient parallel implementation anyway.

As a domain for testing the optimizations we use a half ball with a small box cut out at its bottom. The diameter of the half ball is 6.0, the box has a size of $1.0 \times 2.0 \times 0.3$ (see Figure 10). The domain is discretized with 293 elements on the coarsest mesh, generated by Gmsh [15].

These elements are refined 8 times, which leads to $1.02 \cdot 10^8$ unknowns on the finest level. A well-known degeneracy measure for FE meshes is the ratio between inscribed and circumscribed radius α , another one is the ratio between the shortest and the longest edge β . The average degeneracy measures of our test mesh are $\alpha = 0.610$ and $\beta = 0.537$. The minimal and maximal values are $\alpha_{min} = 0.313$, $\alpha_{max} = 0.900$, $\beta_{min} = 0.214$, and $\beta_{max} = 0.830$.

Figure 10: Test domain: 293 elements on the coarsest mesh.



5.3.1. Unoptimized version and exact block-wise solving

As a reference a four-color smoother is considered in the domain. For the unoptimized version $\nu = (4, 4)$ yielded the best time to solution. With this number of smoothing steps, 21 W- or V-cycles are required to reduce the error of a random initial solution below 10^{-7} . On a single core, one V-cycle takes

approx. 16 seconds. For all following experiments, we measure the convergence rate of the last cycle (see Table 7).

Further we impose two conditions:

1. The required amount of communication is the same for all the methods. We are exchanging eight times all ghost boundary points at the interfaces during the smoothing procedure.
2. The total smoothing workload has to be comparable to the unoptimized version in the solving phase. The additional time for the setup phase strongly depends on the implementation of a LFA evaluation in some of the following smoothing strategies.

The first condition provides an estimate of a tight lower limit for the global convergence rate for our experiments. For standard iterative smoothers, we can estimate this limit by solving each block exactly (see Table 7 *exact block-wise solving*). However this is just to provide a comparison, since it requires much more smoothing work than we need for the unoptimized version. The interface points (macro vertices, edges and faces) between the structured regions are also considered as small blocks in themselves.

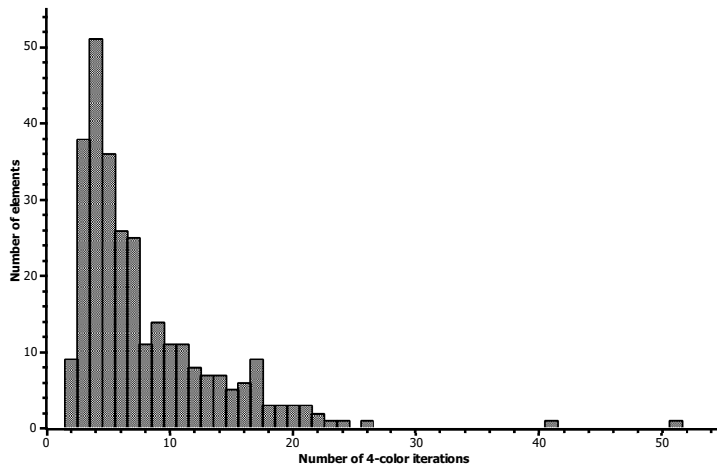
Smoothing strategy	W-cycle	V-cycle	ω
Unoptimized	0.64	0.65	1.0
Exact block-wise solving	0.11	0.18	-
Adaptive smoothing steps	0.51	0.53	1.0
+ Additional interface smoothing	0.34	0.34	1.0
Full damping	0.59	0.56	1.15
Interior damping	0.44	0.49	1.55 / 1.0
+ Additional interface smoothing	0.30	0.30	1.55 / 1.0
Adaptive interior damping	0.46	0.51	variable
+ Additional interface smoothing	0.31	0.34	variable
Combined Methods	0.15	0.19	1.55 / 1.0

Table 7: Measured convergence factors for different smoothing strategies

5.3.2. Locally adaptive number of smoothing steps

LFA predictions can help to adjust the number of relaxation steps according to the element. Since the communication overhead should remain the same, we adjust the smoothing procedure locally. In order to individually increase the amount of smoothing work for a structured region, we add 4-color smoother iterations during smoothing steps. During execution of those iterations, the ghost points of the element are not updated. Thus, it is like smoothing a smaller Dirichlet boundary value problem. We decrease the smoothing work for a structured region by skipping smoothing during a (global) smoothing step.

Figure 11: Histogram of the number of 4-color iterations applied in the structured regions in the adaptive smoothing step version.



For our experiment, the overall smoothing work should stay constant, thus it is more a redistribution of smoothing work. We start by setting the number of smoothing iterations for all structured regions to one. At this stage there is one real update of the ghost layers, but seven (three at pre- and four at post-smoothing) which would not be needed at all. Then all convergence rates are predicted by LFA and the remaining smoothing iterations are successively distributed to the element with the highest convergence rate. After each step the convergence rate of the updated element has to be recalculated. The smoothing iterations are distributed as equally as possible amongst between the updating steps of the ghost boundaries. The LFA evaluation took around 5 seconds for our mesh in the setup time. But the advantage easily outweighs the required time. In table 7 *adaptive smoothing steps* shows the effect of this optimization. For our example, Figure 11 gives an impression of the smoothing work distribution. For most elements $\nu_1 + \nu_2 = 4$ steps are predicted to be sufficient, in an extreme cases even $\nu_1 + \nu_2 = 51$ are predicted for an upper bound of 0.18 on the convergence factor for each single structured region.

Moreover, we can add (local) smoothing iterations for the interface points, too. Since we do not save this additional work anywhere else, it is some overhead. However, it is neglectable compared to its possible effects (see *+ additional interface smoothing* in Table 7), since there are many more inner points than interface points.

5.3.3. Locally adaptive damping

In a first step we want to optimize the damping parameter. A simple choice is a constant damping parameter $\omega_{const} = \omega_1 = \omega_2 = \omega_3 = \omega_4$ for all points (see

full damping in Table 7). By experiment $\omega_{const} = 1.15$ showed up to be a good choice. Damping parameters around 1.25 and more lead to divergence.

These damping parameters are low compared to LFA predicted optimal damping values in the interior of the structured regions. Indeed, the interface points cause a problem in this case. Without damping the interface points we observe improved convergence using a larger damping factor of 1.55 (see *interior damping*, Table 7). Increasing the experimentally found damping parameters on the macro vertices, edges and faces to 1.1 nearly does not improve the convergence rate. Similarly to the optimization in subsection 5.3.2, *additional interface smoothing* is necessary to obtain the full potential of this optimization.

To further improve the damping parameters, we tried to find optimal relaxation parameters for each structured region. The four-color damping parameters are determined by applying the downhill simplex method [27] to LFA individually for each of the 293 elements on the coarsest mesh. This is computationally quite expensive. The optimal damping parameter can vary quite strongly amongst the different stencils. Inside the domain, quite low damping parameters e.g. $\omega = (1.43, 1.26, 1.17, 1.33)$ and large damping parameters e.g. $\omega = (1.75, 1.47, 1.46, 1.83)$ or $\omega = (1.51, 2.00, 1.44, 1.46)$ are applied. However it did not improve the time to solution (see *adaptive interior damping* in Table 7). Exactly the same number of V-cycles like using the global damping parameter are required. The convergence factors are even a bit worse than using *interior damping*. LFA predicts for some structured regions convergence factors down to 0.03, while worst convergence factors are up to 0.51 and 0.36 with and without damping, respectively.

Summarizing, the interface points benefit from additional smoothing. Further, the interior points can be damped more extremely, as long as damping is avoided on the interface points. It was not favorably to choose different damping parameter for the interior points.

5.3.4. Combined methods

In this section, we combine the various methods. As we will see, the positive effects w.r.t. the convergence factor will be additive to some extent. We chose the best variant of each previous subsection 5.3.3 and 5.3.2. Thus, the *combined methods* of Table 7 include *adaptive smoothing steps*, *interior damping*, and *additional interface smoothing*. For this example the convergence rate is even similar to an *exact block-wise solving*.

6. Conclusions

We were able to show a good correspondence between the LFA and HHG for Jacobi, lexicographic and four-color Gauss-Seidel, line- as well as for plane- type smoothers. The variation between the measured results of HHG and the LFA predictions for the asymptotic convergence rate is below 10% in all measured cases. We presented a two-grid analysis for the Laplace operator discretized by linear finite elements on tetrahedral grids. The four-color smoother requires a

decomposition of the Fourier space into minimal invariant subspaces, four and sixteen dimensional for the smoothing and the two-grid analysis, respectively. The four-color smoother was the best choice for regular-like tetrahedra. An optimal choice of individual damping parameters for the different colors has a stronger impact to improve the convergence factor than it is the case for a lexicographic Gauss-Seidel. Line-smoothing shows an especially good convergence for some tetrahedral shapes, e. g. for the wedge type. Plane-smoothing is very efficient for needle or spindle shaped elements. For both multi-relaxation schemes, a zebra-wise updating proved more effective than a lexicographic updating.

The agreement between the LFA and HHG can be seen as a validation for both implementations. Furthermore, benefits of more complex solvers can first be tested with the LFA before implementing them in HHG. This prevents development effort that would be futile, if the solver turned out not to be suitable for HHG.

Considering semi-structured grids, the interfaces between the structured blocks are often used, e. g., as boundaries for a parallelization. Thus points on the boundaries have to be updated before or after the structured parts to keep the communication low. While for point-wise smoothing this proceeding has nearly no influence on the convergence, this is not the case for line- or plane-smoothing. We experienced a strong effect when interfaces separated a collective update in several parts. While an additional smoothing of the interface points and over-relaxation can slightly reduce this effect, further work has to be done for an improvement. On the other hand we could show, with three different smoothers on three degenerated tetrahedral regions, that there is no inherent problem for locally adaptive smoothing. It can be very advantageous to use different smoothing strategies for the different sub-domains.

Because of the refinement strategy in HHG, child elements of a tetrahedron have the same anisotropy as the parent element. Thus, it can be worthwhile doing some calculations in order to find out good smoothing parameters, since these parameters are applied to a huge number of tetrahedrons on the finer grids. In the last part of the paper we focused on the number of pre-/post-smoothing steps and local adaptively chosen damping parameters. It turned out that by redistributing the number of smoothing steps and applying different local damping parameters over a semi-structured test domain can significantly reduce the convergence.

Acknowledgments

This work was partially supported by FEDER/MCYT Projects MTM 2010-16917, the DGA (Grupo consolidado PDIE), by the Kompetenznetzwerk für Technisch-Wissenschaftliches Hoch- und Höchstleistungsrechnen in Bayern (KONWIHR), and the International Doctorate Program (IDK) "Identification, Optimization and Control with Applications in Modern Technologies" within the Elite Network of Bavaria.

References

- [1] R. BARLOW AND D. EVANS. *Synchronous and asynchronous iterative parallel algorithms for linear systems*. Comput. J., 25 (1982), pp. 56–60.
- [2] G. M. BAUDET., *Asynchronous iterative methods for multiprocessors*. J. ACM, 25 (1978), pp. 226–244.
- [3] B. BERGEN, T. GRADL, F. HÜLSEMANN AND U. RÜDE. *A massively parallel multigrid method for finite elements*. Comput. Sci. Eng., 8 (2006), pp. 56–62.
- [4] B. BERGEN, F. HÜLSEMANN AND U. RÜDE. *Towards Petascale Multilevel Finite-Element Solvers* Petascale Computing. Algorithms and Applications, Boca Raton / London / New York, Chapman & Hall/CRC, (2008).
- [5] J. BEY. *Tetrahedral grid refinement*. Computing, 55 (2005), pp. 355–378.
- [6] A. BORZI. *High-order discretization and multigrid solution of elliptic non-linear constrained optimal control problems*. J. Comput. Appl. Math., 200 (2007), pp. 67–85.
- [7] T. BOONEN, J. VAN LENT AND S. VANDEWALLE. *Local Fourier Analysis of multigrid for the curl-curl equation*. SIAM J. Sci. Comput., 30 (2008), pp. 1730–1755.
- [8] A. BRANDT. *Multi-level adaptive solutions to boundary-value problems*. Math. Comput., 31 (1977), pp. 333–390.
- [9] A. BRANDT, S. MCCORMICK AND J. RUGE. *Algebraic multigrid (AMG) for sparse matrix equations*. Sparsity and Its Applications, Cambridge Univ. Press, (1984).
- [10] W. BRIGGS V. E. HENSON, S. MCCORMICK. *A Multigrid Tutorial.*, Society for Industrial and Applied Mathematics, (2000).
- [11] D. CHAZAN AND W. MIRANKER. *Chaotic relaxation* Lin. Algebra App., 2 (1969), pp. 199–222.
- [12] P.M. DE ZEEUW. *Development of semi-coarsening techniques* Appl. Numer. Math., 19 (1996), pp. 433–465.
- [13] F.J. GASPAR, J.L. GRACIA AND F.J. LISBONA. *Fourier Analysis for Multigrid Methods on Triangular Grids*. SIAM J. Sci. Comput., 31 (2009), pp. 2081–2102.
- [14] F.J. GASPAR, J.L. GRACIA, F.J. LISBONA AND C. RODRIGO. *Multigrid finite element methods on semi-structured triangular grids for planar elasticity*. Num. Lin. Algebra App., 17 (2010), pp. 473–493.

- [15] C. GEUZAINÉ AND J.-F. REMACLE. *Gmsh: a three-dimensional finite element mesh generator with built-in pre- and post-processing facilities*. Int. J. for Num. Methods in Eng., 79 (2009), pp. 1309–1331.
- [16] B. GMEINER, T. GRADL, H. KÖSTLER AND U. RÜDE. *Highly Parallel Geometric Multigrid Algorithm for Hierarchical Hybrid Grids*. NIC Symposium 2012, Publication series of the John von Neumann Institute for Computing, vol. 45, K. Binder, G. Münster, M. Kremer (eds.), Jülich, Germany, 2012; pp. 232–330.
- [17] T. GRADL AND U. RÜDE. *High Performance Multigrid on Current Large Scale Parallel Computers*. 9th Workshop on Parallel Systems and Algorithm (PASA), Bonn, (2008).
- [18] W. HACKBUSCH. *Multi-grid methods and applications*. Springer, Berlin, 1985.
- [19] P.W. HEMKER, W. HOFFMANN AND M.H. VAN RAALTE. *Two-level Fourier analysis of a multigrid approach for discontinuous Galerkin discretizations*. SIAM J. Sci. Comput., 25 (2003), pp. 1018–1041.
- [20] V.E. HENSON AND U.M. YANG. *BoomerAMG: a parallel algebraic multigrid solver and preconditioner*. Applied Numerical Mathematics, 41 (2002), pp. 155–177.
- [21] R. HOCKNEY. *A fast direct solution of Poisson's equation using Fourier analysis*. J. ACM, 12 (1965), pp. 95–113.
- [22] F. HÜLSEMANN, M. KOWARSCHIK, M. MOHR AND U. RÜDE. *Parallel Geometric Multigrid*. Numerical Solution of Partial Differential Equations on Parallel Computers, 51 of LNCSE (2005), pp. 165–208.
- [23] C.-C.J. KUO AND B.C. LEVY. *Two-color Fourier analysis of the multigrid method with red-black Gauss-Seidel smoothing*. Appl. Math. Comput., 29 (1989), pp. 69–87.
- [24] MICHAL KRIZEK. *On the maximum angle condition for linear tetrahedral elements*. Siam J. on Numer. Anal., 29 (2) 513–520 (1992)
- [25] I. M. LLORENTE AND N. D. MELSON. *Behavior of plane relaxation methods as multigrid smoothers*. Electr. Trans. on Numer. Anal. 10 (2000), pp. 92–114.
- [26] J. D. MOULTON, J.E. DENDY AND J.M. HYMAN. *The black box multigrid numerical homogenization algorithm*. J. of Comput. Physics 142 (1998), pp. 80–108.
- [27] C.-C.J. KUO AND B.C. LEVY. *A Simplex Method for Function Minimization*. Computer J., 7 (1965), pp. 308–313.

- [28] C.W. OOSTERLEE. *The convergence of parallel multiblock multigrid methods*. Appl. Numer. Math., 19 (1995), pp. 115–128.
- [29] J.W. RUGE AND K. STÜBEN. *Algebraic multigrid (AMG)*. Frontiers in Appl. Math., 3 (1987), pp. 73-130.
- [30] J.R. SHEWCHUK. *What Is a Good Linear Finite Element? - Interpolation, Conditioning, Anisotropy, and Quality Measures*. In Proc. of the 11th International Meshing Roundtable (2002).
- [31] K. STÜBEN. *A review of algebraic multigrid*, J. Comput. Appl. Math., 128 (2001), pp. 281–309.
- [32] U. TROTTEBERG, C.W. OOSTERLEE AND A. SCHÜLLER. *Multigrid* Academic Press, New York, 2001.
- [33] P. WESSELING. *An introduction to multigrid methods*. John Wiley, Chichester, UK, 1992.
- [34] R. WIENANDS AND W. JOPPICH. *Practical Fourier analysis for multigrid methods*. Chapman and Hall/CRC Press, 2005.
- [35] R. WIENANDS, C.W. OOSTERLEE AND T. WASHIO. *Fourier analysis of GMRES(m) preconditioned by multigrid*. SIAM J. Sci. Comput., 22 (2000), pp. 582–603.
- [36] I. YAVNEH. *Multigrid smoothing factors for red-black Gauss-Seidel relaxation applied to a class of elliptic operators*. SIAM J. Numer. Anal., 32 (1995), pp. 1126–1138.
- [37] I. YAVNEH. *On red-black SOR smoothing in multigrid*. SIAM J. Sci. Comput. 17 (1996), pp. 180–192.
- [38] G. ZHOU AND S.R. FULTON. *Fourier analysis of multigrid methods on hexagonal grids*. SIAM J. Sci. Comput. 31 (2009), pp. 1518–1538.